JOURNAL OF AIRCRAFT
Vol. 43, No. 6, November–December 2006

Phase-Locked Particle Image Velocimetry Measurements of a Flapping Wing

Manikandan Ramasamy* and J. Gordon Leishman†
University of Maryland, College Park, Maryland 20742

DOI: 10.2514/1.21347

The unsteady aerodynamics of a biomimetic inspired flapping-wing mechanism has been analyzed by performing detailed phase-locked diagnostics of its flow field. Flow visualization and particle image velocimetry results have shown the presence of a shed dynamic stall vortex that spans across most of the wing span. The shedding of this type of leading-edge vortex was accompanied by the formation of another leading-edge vortex before the first vortex reached the midchord, resulting in multiple shedding leading-edge vortices on the top surface of the wing during each wing stroke. A strong starting vortex was also formed at the trailing edge of the wing during the early part of its translational stroke. This vortex continuously gained strength from shed vorticity as the wing accelerated into its stroke. The starting vortex remained close to the trailing edge until the wing reached midstroke. A pair of vortices that continuously trailed from the root and tip of the wing were identified, both of which induced a significant downwash velocity over the wing surface. These trailed vortices were found to exhibit a contracting wake structure as they convected into the wake below the wing, consistent with an increase in slipstream velocity. The evolution of the tip and root vortex pair showed rapid diffusive characteristics with an increase in time (wake age).

Nomenclature

a, a_1 = constants
b = wing semispan, m
c = wing chord, m
$\bar{c}$ = mean aerodynamic chord, m
r_0 = initial core radius of the vortex, m
r_c = core radius of the vortex, m
r = radial distance, m
$\bar{r}$ = nondimensional radial distance, $=r/r_c$
Re = Reynolds number, $=\rho V\bar{c}/\nu$
Re_v = vortex Reynolds number, $=\Gamma_v/\nu$
Ri = Richardson number
V = free stream velocity, $\mathrm{m^2/s}$
V_{tip} = tip velocity of the flapping wing, m/s
V_θ = swirl velocity of the root and tip vortices, m/s
α = Lamb's constant, $=1.25643$
Γ_v = vortex circulation, $=2\pi r V_\theta$, $\mathrm{m^2/s}$
δ = ratio of apparent to actual viscosity
ζ = wake age, deg
ν = kinematic viscosity, $\mathrm{m^2/s}$
ν_t = eddy viscosity
ν_T = total viscosity, $=\nu+\nu_t$
θ = pitch angle of the flapping wing, rad
$\dot{\theta}$ = pitch rate of the flapping wing, rad/s
ρ = air density, $\mathrm{kg/m^3}$
ψ = phase angle in the flapping cycle, deg
Ω = frequency of flapping, Hz

Introduction

SCIENTIFIC interest continues to increase in hover-capable microair vehicles (MAV). MAVs have civil and military potential for investigating dull, dirty, and dangerous environments. This is especially true in military missions, such as reconnaissance into hostile territory, where the risk of endangering human life can be reduced. MAVs can be used for many types of scouting purposes, especially when the environment is filled with chemical and biological agents.

Two different concepts (flapping wings and rotating wings) are being considered for application to hovering MAVs. Thus far at least, rotating wings have shown low efficiencies at MAV scale, mainly because of high profile and induced losses associated with ultralow Reynolds number operation [1,2]. Insects, with their flapping wings, seem to have found a way to use effectively complicated three-dimensional vortical flows and unsteady aerodynamic effects to produce substantial performance even at very low Reynolds numbers. Although the problem has been examined experimentally, successfully developing a biomimetic flapping wing has its difficulties not only from the ability of the analyst to reproduce the kinematics and aeroelastics of insect wings, but also by fully interrogating the flow field to gain a comprehensive knowledge of its aerodynamics. This understanding may allow MAV designers to exploit the complex, but potentially useful, aerodynamic phenomena used by insects.

The aerodynamic flow field surrounding flapping wings has been analyzed over several decades by using living insects, mechanical models, and numerical flow simulations. Experiments performed using living insects [3,4] have met with only limited success in understanding the flows from a fundamental fluid mechanics perspective. This is also because of the difficulties in separating aerodynamic forces from inertial and aeroelastic forces [5,6]. Furthermore, the issues in making detailed quantitative measurements on a living insect under controlled conditions are just too complex. As a result, mechanical models that mimic the wing motion have been built to make measurements that help more fully understand the underlying physics of flapping-wing-borne flight [7–11]. However, the intricate aeroelasticity issues associated with the deforming wing and the effects on the resulting aerodynamics are not well understood, nor can they be easily replicated. The difficulties in building a mechanism to operate a large-scale flapping-wing model at a sufficiently high required reduced frequency also makes the problem very challenging.

Minotti [12] attempted theoretically to estimate the forces produced by a flapping wing that has a complex three-dimensional flow field using various assumptions, which included two-dimensional, inviscid flow. Deducing empirical coefficients from experiments, the predictions of the model correlated relatively well

---

Received 23 November 2005; revision received 25 June 2006; accepted for publication 26 June 2006.

*Assistant Research Scientist, Department of Aerospace Engineering; mani@umd.edu. Member AIAA.

†Minta Martin Professor of Engineering, Department of Aerospace Engineering; leishman@eng.umd.edu. Associate Fellow AIAA.

with the measurements. However, extending this work to account for real flow field conditions imposes considerable numerical challenges. Using computational fluid dynamic models to understand the flapping-wing flow field [13–15], has thus far provided only limited additional physical insight to the problems. This is mainly because of the difficulties in modeling turbulence and in preserving the three-dimensional wake vorticity to relatively old ages in terms of wing flapping cycles.

Making measurements in the flow field of a flapping wing is also particularly challenging. The flow is filled with small-scale, vortical structures, with steep velocity gradients, which raises measurement resolution issues, both spatial and temporal [16]. The combination of high angle of attack and low Reynolds numbers on a flapping wing results in significant regions of flow separation. Also, the reciprocating motion of the wing in the stroke plane has varying translation and angular velocities (accelerating in the early part of translation, followed by deceleration with high angular wing motion rates when translation stops). As a result, there are large changes in the aerodynamic loads on the wing, which have their origin in both circulatory as well as noncirculatory (apparent mass) effects. Combined with flow separation and vorticity development, measuring the airloads and defining the three-dimensional flow field becomes very difficult because it must be synchronized (phase locked) with the wing stroke location. For example, the strength of the leading-edge vortex (LEV), which is hypothesized to play a significant role in overall lift generation on flapping wings, depends directly on the wing stroke location. Also, the spatial location of the root and tip vortices relative to the wing, their strength, and their convection velocities will all be a function of the wing stroke location.

Despite these complexities, several hypotheses have been put forth by researchers to try to explain the physics behind the flapping wings. Because conventional, linear, quasisteady aerodynamics [15,17] has failed to explain the lift characteristics exhibited by flapping-wing insects, various nonlinear, unsteady flow mechanisms have been proposed. For example, Weis–Fogh [18] suggested that a mechanism called "clap and fling" is responsible for lift production. Other variations of this mechanism include "clap and peel" and "near-clap and fling." This requires the insects to have a 180 deg flapping stroke, yet because most insects do not have such a large flapping stroke, this cannot explain the lift levels produced [19]. Ellington et al. [10] suggested that insects generate enhanced lift using a spilled leading-edge vortex (LEV) that arises from the combination of high angle of attack and low Reynolds number. The presence of a LEV was identified from flow visualization on a hovering hawk moth *Manduca Sexta* [3], and also on a mechanical "flapper" that mimicked the wing movements of the hawk moth at an operating wing tip Reynolds number of 1,500 [20,21].

A LEV is expected to be shed as it gains energy from a shear layer produced by the continuous translation of the wing in the stroke plane. However, Ellington made the observation that the LEV remains attached during most part of the flapping-wing cycle at very low Reynolds numbers [10]. This requires a delicate balance between the generation of vorticity at the leading edge and the transport of the vorticity into the wake. It was also claimed that a spanwise flow (from root to tip) prevents the LEV from gaining more energy and, as a result, prevents its shedding from the wing. Clearly, the continuous presence of a LEV on top of the wing reduces the pressure on the top surface of the wing and enhances the overall lift produced, although it must also increase wing drag. By performing measurements on a rotating wing (to eliminate the unsteady effects of flapping wing) at different Reynolds numbers (10,000 to 50,000), Ellington and Usherwood [22] found that the lift coefficients at higher Reynolds numbers dropped significantly compared with those at low Reynolds numbers. This perhaps suggests the less pronounced formation of LEVs at higher Reynolds numbers, which is where MAVs operate. Birch and Dickinson [23] suggested that different mechanisms are responsible for the stability of the LEV at different Reynolds numbers. They hypothesized that for Reynolds numbers relevant to insects ($Re = 150$), a downward flow induced by the wing tip vortices would be the primary source that limits the growth of the LEV, not the spanwise flow. This hypothesis was based on the results from an experiment where the spanwise flow of the flapping wing was restricted using fences and baffles.

It is apparent from the foregoing that the effect of Reynolds number on the stability of LEVs, or on their mere existence, is still not clear. It is, therefore, essential to have a better understanding of Reynolds number effects because the operating Reynolds number for flapping-wing MAVs ($Re = 10^3$ to 10^5) is much higher than that found with living insects ($Re \approx 150$). The flow field observations that are made at very low Reynolds number may be different or may not even exist at the operating Reynolds numbers of MAVs. Also, it is apparent from the literature that the trailed vortex system has never been taken into account when explaining the aerodynamic characteristics of flapping wings. This suggests the need for much more fundamental research on flapping wings, including high-resolution quantitative flow field measurements, which can help better understand their complex flow structure and can be used for validation of predictive models.

The specific objectives of the present study were to develop effective techniques to allow high-fidelity flow measurements in the flow field of a flapping wing, and to further a fundamental understanding of its overall aerodynamics. Detailed flow visualization and particle image velocimetry (PIV) measurements were made to understand the evolutional properties of the vortices trailing from the wing tip and wing root. The work included several important new observations, including the substantial role of turbulence, even at such low Reynolds numbers.

Experimental Setup

A biomimetic, insect-based, flapping-wing mechanism has been built at the University of Maryland, which has been used for several prior studies [24–26]. The mechanism is capable of approximately emulating the reciprocating kinematics of insect wings. A typical wing motion that is shown in Fig. 1, which was measured from the flapping-wing mechanism used in the current study. The motion consists of four parts: 1) a downstroke, in which the wing translates with a constant pitch angle; 2) supination, where the wing rotates through a large angle of attack range to produce a positive pitch angle on the upstroke; 3) upstroke, which again is a translation motion with constant pitch angle; and 4) pronation at the end of the upstroke, where the wing rotates back again to have a positive pitch angle during the downstroke. It can be seen from Fig. 1 that the pitch angle and pitch rate are a function of the stroke location during the flapping cycle.

Figure 2 shows the photograph of the flapping-wing mechanism used in the current study. The motion was produced by a brushless motor, which was controlled by a sensorless speed controller. This was operated in combination with a microprocessor-based precision pulse generator. The motor shaft was rigidly attached to a rotating disk, which in turn was attached to a pin that drove a scotch yoke. As the shaft was actively flapped, pitch actuators, which are rigidly

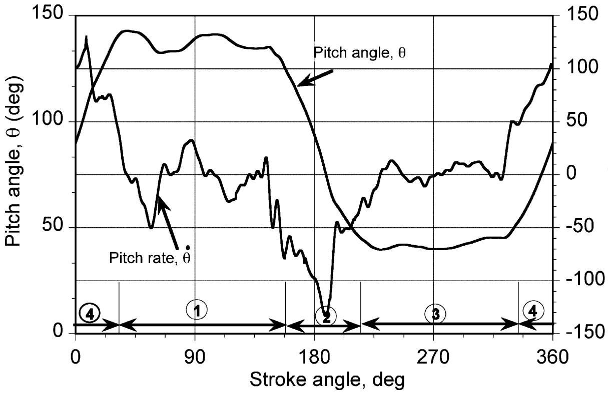

Fig. 1 Wing kinematics for one full cycle: 1) downstroke; 2) supination; 3) upstroke; 4) pronation.

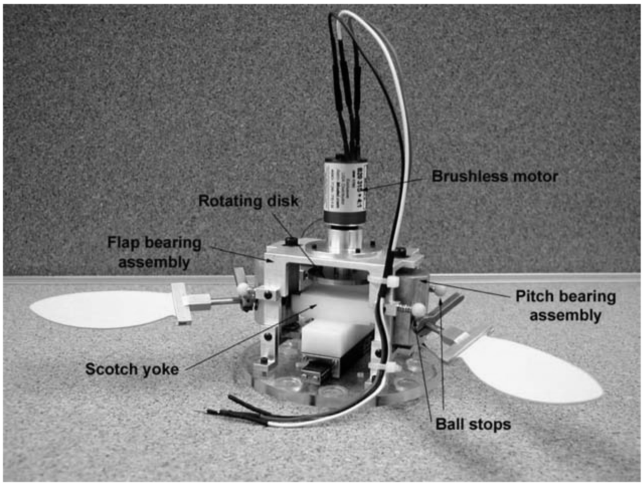

Fig. 2 Insect-based flapping-wing model developed at University of Maryland [24].

attached to the wing shaft, made contact with Delrin ball ends at the end of each half-stroke. This caused the shaft to pitch and, hence, to generate the supination and pronation wing motion at the end of each flapping stroke.

The rotation of the shaft and supination/pronation is generated by the pitch assembly, which also serves to fix the pitch angle of the shaft during the translational phases of the wing motion [24]. The pitch assembly consists of a main shaft that is rigidly attached to the cam and is, in turn, held by a slider and compression spring. In combination with the pitch stop, the entire assembly is bistable in that it allows the shaft to rest in only two positions. The model has a 80 deg flapping stroke in the horizontal plane. Further details on the operation of the mechanism are given in [24].

Aluminum/mylar wings were attached to the flapping-wing mechanism, the planform of which is based on a scaled-up fruit fly wing (similar to the Robofly wings in [9]), as shown in Fig. 3. The wing was made using a 0.5 mm thick aluminum frame. The maximum pitch angle of the flapping wing during the translational stroke was set to 45 deg. The operating Reynolds number based on maximum stroke velocity and mean aerodynamic chord was approximately 15,500.

The flapping-wing model was mounted on a test stand at about ten effective wing spans from the ground. The experimental apparatus was placed inside a flow conditioned test cell of volume 362 m^3. Because the flapping-wing model was tested with a single semispan wing in the present work, a large image plane was constructed to provide symmetry to the flow, as shown in Fig. 4.

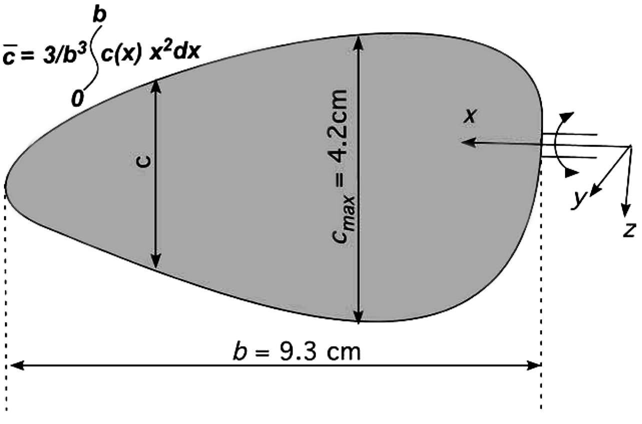

Fig. 3 Schematic of the flapping wing used in the experiment.

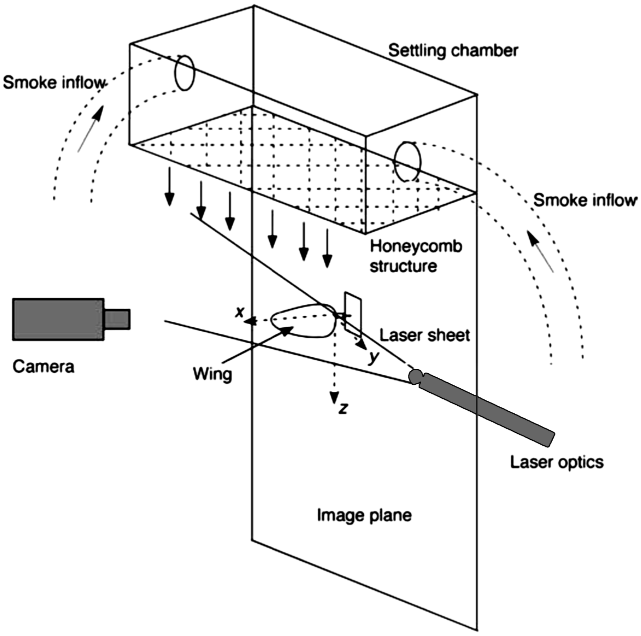

Fig. 4 Schematic of the experimental apparatus used for the flapping-wing studies.

Flow Visualization

Flow visualization images were acquired by seeding the flow using a mineral oil fog strobed with a laser sheet. This light sheet was produced by a dual Nd:YAG laser and was located in the desired orientation in the flow using an optical arm. Images were acquired using a 6.1 megapixel digital camera with its optical axis placed perpendicular to the laser light sheet. The laser was triggered using a once-per-revolution signal, which was obtained from an encoder attached to the flapping mechanism. The laser light sheet was placed parallel to the span of the wing to capture the root and tip vortices, and was placed along the chord at different span locations to capture the images of the LEVs. A phase delay was introduced so that the laser could be fired at any flapping phase angle. A schematic explaining the experimental apparatus used for the flow visualization is shown in Fig. 4.

Seed was produced by vaporizing a mineral oil into a dense fog. Oil was broken down into a fine mist by adding nitrogen under pressure, forced into a heater block, and heated to its boiling point where it became vaporized. As the vapor escaped from the heat exchanger nozzle, it was mixed with ambient air, rapidly cooled, and condensed into a fog. The fog/air mixture was passed through a series of ducts and introduced into the flapping-wing flow field using a plenum and honeycomb settling chamber, as shown in Fig. 4. The plenum reduces the velocity of the smoke that enters the measurement flow field to such an extent that the smoke never reaches the region of focus unless the flapping-wing mechanism is operating and inducing a flow. The honeycomb screens help ensure that the incoming flow is almost eddy free.

Particle Image Velocimetry System

The important parts of the PIV system included a pulsed laser light sheet for illuminating the region of focus in the flow field (described previously), a CCD camera to acquire the images, and a calibration grid to obtain quantitative values from the acquired images. The camera was operated synchronously with the laser in double exposure mode to acquire two noninterlaced full frame images during a single frame interval. Images were acquired using a 8-bit CCD camera having a sensor array of 1K-by-1K (1 MP) pixels.

To measure the flow field in a plane perpendicular to the stroke plane of the flapping wing, the camera was focused on the laser light sheet located along the wing span. The camera covered the region of interest, which was 135 mm-by-100 mm. This means that each pixel is a distance of about 0.1318 mm and 0.0976 mm in the *x* axis and *y* axis, respectively. A grid of 81 horizontal nodes by 60 vertical nodes was constructed in the aforementioned region of interest; this resulted in a distance of 1.6 mm between adjacent nodes in either direction. A laser pulse separation delay of 30 μs for a fluid flow of approximately 8 m/s (maximum tip velocity of the flapping-wing) will result in 0.24 mm movement of the individual seed particles. This is well within the 1.6 mm distance between the adjacent nodes. A correlation based on adaptive grid principles is used in the present study and care was taken to minimize the number of interpolated vectors in each image. The limitations, uncertainties, and specific challenges associated with using PIV for velocity measurements in such a complex flow field have been discussed in [16]

Results

The measurements that were performed to understand the flow field surrounding the flapping wing are discussed under the following two categories: 1) chordwise measurements, and 2) spanwise measurements. The optical axis of the camera was placed perpendicular to the laser light sheet for both the flow visualization and the PIV measurements. In the case of the chordwise flow visualization, as the laser light sheet was projected either from the right- or left-hand sides, and so a shadow appears behind the wing. The wing phase, ψ, is represented in such a way that the entire flapping stroke (supination, downstroke, pronation, and upstroke) is of 360 deg, with 0 deg representing the midpoint of supination and 180 deg representing the midpoint of pronation.

Chordwise Measurements

Figure 5 shows examples of phase-locked flow visualization images that were acquired at a fixed span location (50% of the half-span) through the half-stroke of the wing motion. The region of focus can be appreciated with reference to the schematic shown in Fig. 5a. At $\psi = 0$ (midpoint of supination), the flow over the wing is clearly stalled, as seen in Fig. 5b, with large-scale flow separation, and there are no coherent aerodynamic structures. As the wing continues to supinate, shed vortices from the trailing edge of the wing can be observed in Fig. 5c. Following supination, the wing starts to accelerate into the downstroke, which is accompanied by the formation of a classical “starting” vortex near the trailing edge of the wing; see Fig. 5d. The formation of a strong LEV, which has its source from dynamically increasing high wing angle of attack and the low Reynolds number, occurs at around $\psi = 40$ deg. The size of both the starting vortex and the LEV increases until the wing reaches the midpoint of its translational stroke; see Figs. 5e and 5f.

As the wing continues through its translational stroke, the LEV gains strength and starts moving aft across the chord, as shown in Fig. 5g. This clearly suggests that the LEV is not stable on the wing (directly contradicting the “stable” LEV concept universally proposed by other researchers), and instead exhibits a behavior similar to the known classic features of dynamic stall [27]. This difference may be attributed, at least in part, to the somewhat higher Reynolds numbers at which the flapping-wing mechanism is operated in the current study ($Re \approx 15,500$) when compared with the flapping-wing mechanisms used by both Ellington, Dickinson, and others ($Re \approx 150$ to $1,400$). Research on the problem of dynamic stall on wings when operated at higher Reynolds numbers shows that an aft movement of the LEV will result in elevated lift, followed by abrupt lift stall and then moment stall. There will be a significant reduction in lift when the LEV sheds from the trailing-edge. However, the physics are clearly different in the case of a flapping wing because as soon as the LEV starts to move aft over the chord of the wing, a new spilled vortex simultaneously forms at the leading-edge. This results in multiple vortices on top of the wing

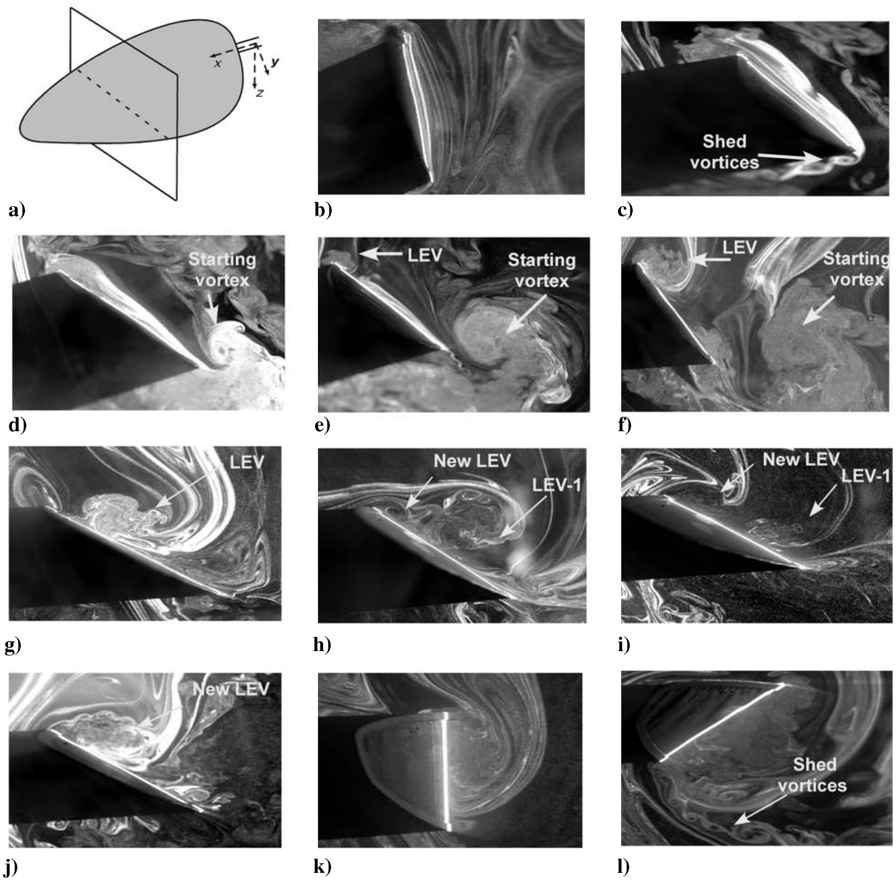

Fig. 5 Chordwise flow visualization images acquired in the flapping-wing flow field during the downstroke: a) schematic explaining the region of focus; b) midpoint of supination, $\psi = 0$ deg; c) during supination, $\psi = 13$ deg; d) start of translational stroke; e) accelerating wing, $\psi = 40$ deg; f) midpoint of translational motion, $\psi = 90$ deg; g) spilled LEV, $\psi = 107$ deg; h) formation of a new LEV, $\psi = 117$ deg; i) multiple vortices, $\psi = 137$ deg; j) second LEV after first one sheds, $\psi = 153$ deg; k) midpoint of pronation, $\psi = 180$ deg; l) shed vortices during pronation, $\psi = 196$ deg.

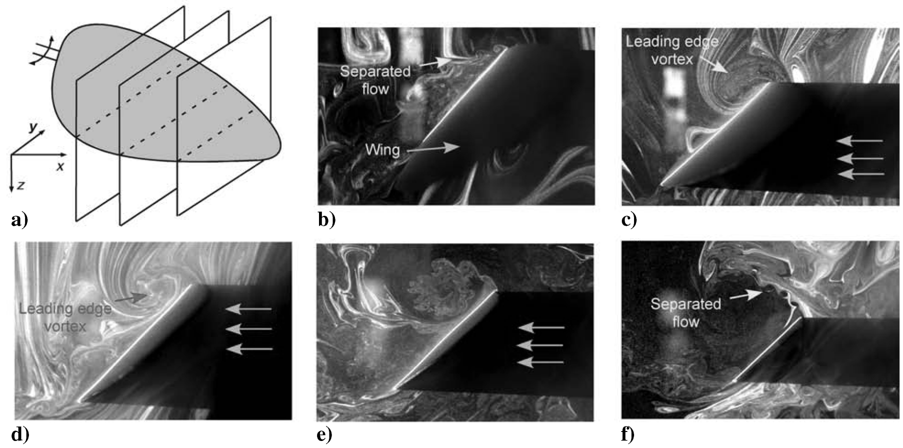

Fig. 6 Chordwise flow visualization images along the span at midpoint of translation: a) schematic showing the region of focus; b) at the root of the wing; c) 20% span location; d) 40% span location; e) 75% span location; f) 85% span location.

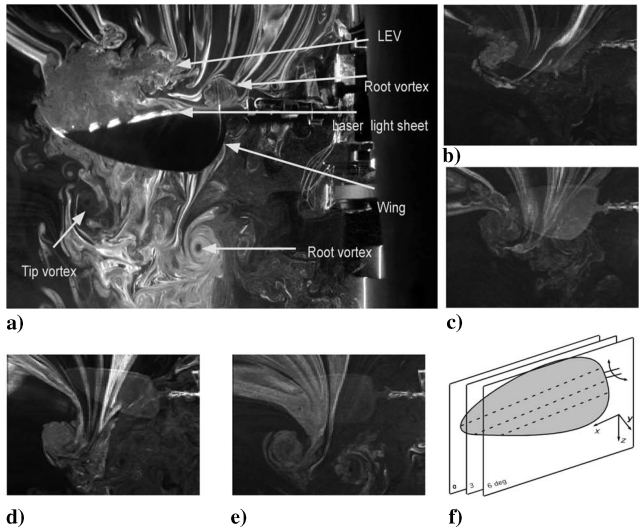

Fig. 7 Root and tip vortices behind the flapping wing at various wake ages: a) $\zeta = 0$ deg; b) $\zeta = 55$ deg; c) $\zeta = 70$ deg; d) $\zeta = 135$ deg; e) $\zeta = 160$ deg; f) schematic explaining the region of focus.

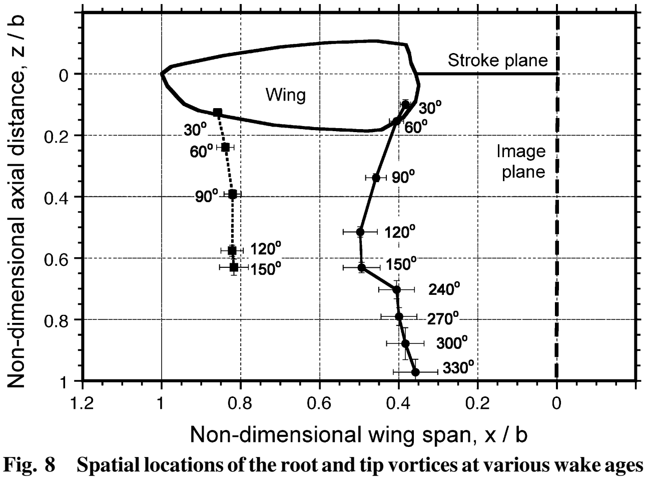

Fig. 8 Spatial locations of the root and tip vortices at various wake ages in the midstroke plane.

surface at any given stroke location; see Figs. 5h and 5i. By this mechanism, wing lift will be sustained throughout the cycle without significant moment stall. Later, the first LEV sheds off from the trailing edge, which is followed by the second LEV as the flapping cycle continues; see Figs. 5j–5l.

The presence of a LEV along the span was verified by acquiring flow visualization images at different span positions for a given stroke location (midstroke). These results are shown in Fig. 6. Except near the extreme root and extreme tip of the wing, the LEV was clearly identifiable across the span. The locally separated flow near the wing tip may be attributed, in part, to the increased local angle of attack that results from elastic wing bending.

Spanwise Measurements

Spanwise flow visualization images were obtained by placing the laser light sheet orthogonal to the stroke plane of the flapping wing at midstroke. The results in this paper are explained in terms of a wake age ζ, which is defined as the time elapsed since the wing reference axis was aligned with the laser light sheet; see Fig. 7f. A wake age of 0 deg would mean that the wing shaft axis is in line with the laser light sheet, and a wake age of 90 deg means that the wing shaft axis has moved through one-quarter of the flapping cycle from the plane of the laser light sheet.

Images acquired behind the trailing edge of the wing, which are shown in Fig. 7, showed the existence of a root and tip vortex pair. The images, which were acquired for the entire flapping cycle, clearly showed the proximity of the root and tip vortex pair to the plane of flapping. Numerous images were acquired for different wake ages, and the locations of the vortex pair were digitized with reference to a calibration grid, which are shown in Fig. 8. Notice that the root and tip vortices convect radially toward each other, and simultaneously convect axially downward with increasing time, suggesting a contracting wake structure. Because there is always an inherent amount of aperiodicity associated with this type of unsteady flow, both the average and the standard deviation of these trailed vortex locations are shown in Fig. 8. The contracting wake structure clearly indicates the increased slip stream velocities and the positive lift produced by the flapping wing [27]. These vortices are also of sufficient proximity to each other that they produce mutually induced effects on their resulting convection through the flow.

Particle Image Velocimetry Measurements

Two digital PIV images from the region of focus in the flapping-wing flow field were acquired with 30 μs phase delay, and were cross correlated to obtain the velocity field. Eighty such pairs were used to obtain an ensemble phase-average of the velocity field. Such velocity vector fields obtained at three different wake ages are shown in Fig. 9. The vortexlike velocity vectors on top of the wing, which are directed toward the wing tip for increasing wake age, suggest that the LEV is considerably three dimensional and is slightly inclined to the wing shaft axis. The spanwise flow in the LEV was found to be significant, and the maximum flow velocity has approximately the same magnitude as the maximum wing tip velocity during the flapping cycle. This spanwise flow has been hypothesized by Van

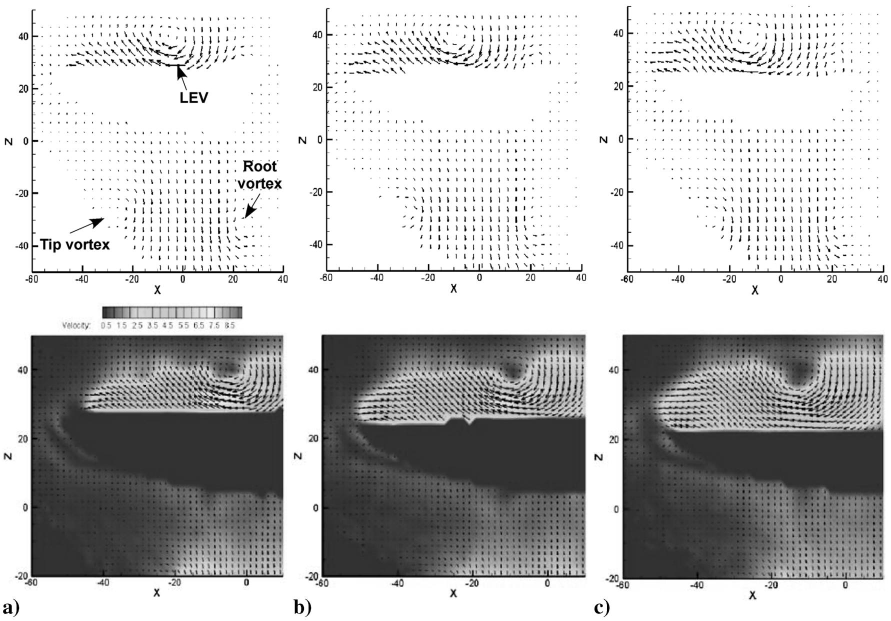

a) b) c)

Fig. 9 PIV analysis for three different wake ages showing the flow field surrounding the flapping-wing surface: a) $\zeta = 0$ deg; b) $\zeta = 3$ deg; c) $\zeta = 6$ deg.

den Berg and Ellington [21] to be the source for the continuous attachment of LEV during the flapping cycle. However, in the present case, the LEV did not stay attached to the wing, as alluded to previously.

A schematic of the overall flow structure on top of the flapping wing, which is based on interpretations of both the flow visualization and PIV analysis, is shown in Fig. 10. Despite the presence of such a significant amount of spanwise flow, the LEVs were found to continuously shed from the upper surface of the wing. This would mean either that the spanwise flow is not large enough to prevent the shedding at this Reynolds number, or that the spanwise flow is not responsible for the continuous attachment of the LEV.

Figure 11 shows the velocity vector fields measured at six different wake ages. It can be observed that the peak induced velocity of the root and tip vortices decrease with increasing wake age. Also, it is confirmed that the trailed root and tip vortices move toward each other and axially downward to give a contracting wake structure, as suggested previously from the flow visualization.

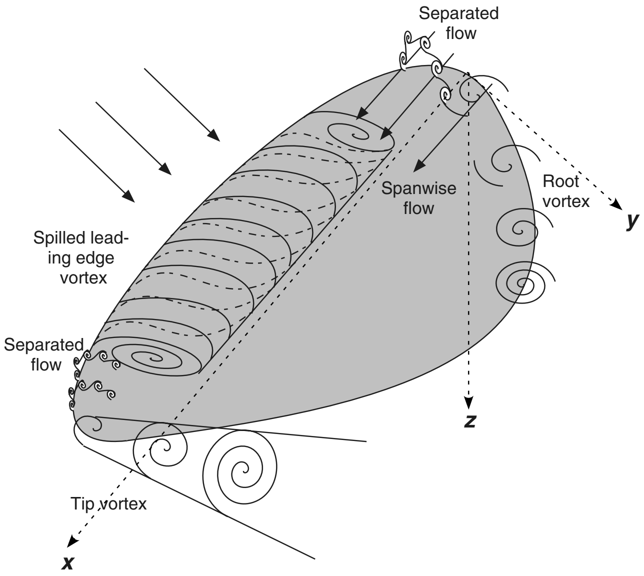

Fig. 10 Schematic of the three-dimensional flow over the top of the flapping wing.

Wake Diagnostics

The importance of the trailed wake system cannot be underestimated because it substantially defines the induced angle of attack of the wing. The measured swirl velocity distribution in both the root and tip vortices at a wake age of $\zeta = 55$ deg is shown in Fig. 12. Note that these profiles were obtained after removing the respective average convection velocities of the vortices through the flow, that is, a Galilean type of velocity field decomposition. The results, therefore, are presented in a frame of reference moving with the vortex core. It can be seen that the tip vortex is stronger than the root vortex, as would be expected, and it has a peak swirl velocity that is 36% of the maximum wing tip velocity. This is a substantial relative velocity, and it clearly has a significant effect on the induced velocity distribution over the wing.

The swirl velocity distribution at various wake ages obtained from the PIV vector plots are shown in Figs. 13 and 14 for the tip vortex and root vortex, respectively. Here, the swirl velocity is normalized using the maximum tip velocity of the wing during its flapping cycle, and the spanwise distance is normalized using the wing span. The core radius, which is half the distance between the swirl velocity peaks, increases with an increase in time, which represents the diffusion of vorticity away from the vortex axis. This is accompanied by a reduction in the peak swirl velocity to conserve circulation. It should be noted that the peak swirl velocity of the tip vortex is about 25% of the maximum wing tip speed even at 160 deg of wake age.

Trailed Vortex Core

Figure 15 shows the measured viscous core size of the tip vortices at various wake ages, which grows logarithmically. Several analytical and semiempirical vortex models have been developed to approximate the growth properties of tip vortices. Among other models, Squire's core growth model [28] has been widely used because of its ability to account for the average effects of turbulence present inside the vortices. In this case the core growth is

$$r_c = \sqrt{r_0^2 + 4\alpha\nu\delta\left(\frac{\zeta}{\Omega}\right)} \tag{1}$$

where δ is given by

$$\delta = 1 + a_1 Re_v \tag{2}$$

and where Re_v is defined by

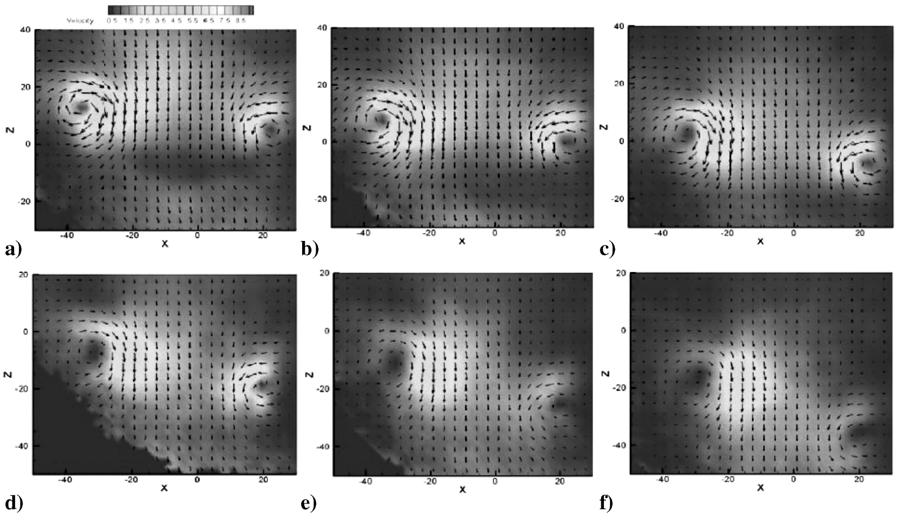

Fig. 11 PIV analysis for different wake ages showing the evolution of root and tip vortices trailing the flapping wing: a) $\zeta = 55$ deg; b) $\zeta = 70$ deg; c) $\zeta = 90$ deg; d) $\zeta = 120$ deg; e) $\zeta = 135$ deg; f) $\zeta = 160$ deg.

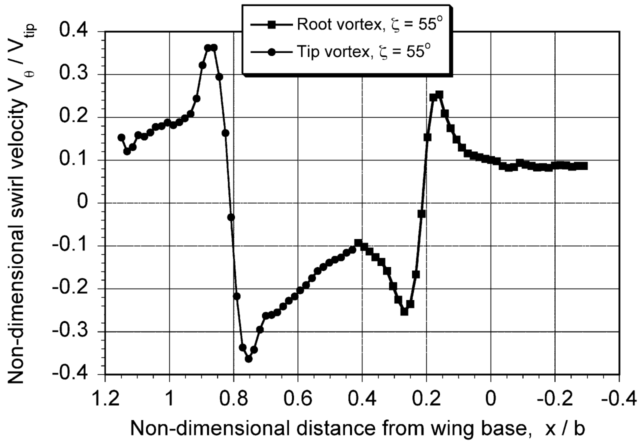

Fig. 12 Swirl velocity profiles for both root and tip vortices at 55 deg wake age.

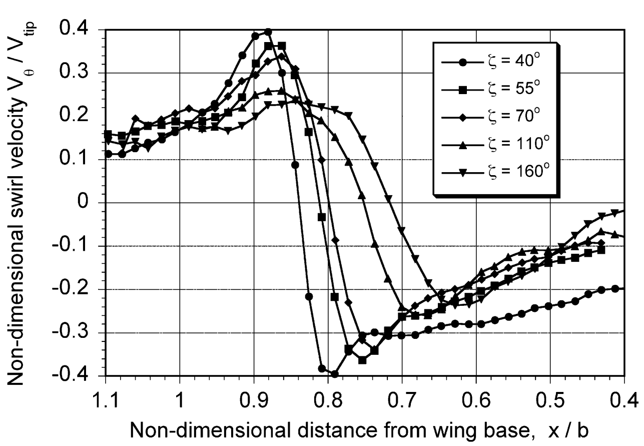

Fig. 13 Swirl velocity profiles of tip vortices at various wake ages.

$$Re_v = \frac{\Gamma_v}{\nu} \tag{3}$$

Equation (1) suggests that an increase in vortex Reynolds number results an increase in the growth rate of the vortices. A value of $\delta = 1$ recovers the laminar Lamb–Oseen model [29,30]. However, it can be seen from Fig. 15 that the measured core growth of the tip vortices from the flapping wing are much higher than this. Substituting a value of $\delta = 250$ in the Squire core growth model predicts the growth rate, whereas a value of $\delta = 8$ is sufficient to predict the measured growth of rotating-wing tip vortex cores. This suggests that the Reynolds number scaling given by Eq. (2) probably does not apply at this scale.

The susceptibility of a vortex entraining turbulence inside its core has been studied in terms of a local gradient Richardson number [31,32]. The original definition of the Richardson number was given by Bradshaw [33] and was modified by Holzapfel [34]. The Richardson number is generally defined as the ratio of turbulence produced/consumed as a result of centrifugal forces (from rotation) to the turbulence produced from shear, that is,

$$Ri = \left(\frac{2V_\theta}{r^2}\frac{\partial(V_\theta r)}{\partial r}\right) \bigg/ \left(r\frac{\partial(V_\theta / r)}{\partial r}\right)^2 \tag{4}$$

Cotel and Breidenthal [35] and Cotel [36] suggested that a small region inside the vortex core remains laminar until the measured local gradient Richardson number stays above a threshold value. This threshold value was found to be dependent on the vortex Reynolds number (which was defined as $Ri_{\text{crit}} = Re_v^{1/4}$). This means that the vortex cannot develop or sustain turbulence until the local Richardson number is above Ri_{crit}.

The variation of Richardson number for the vortices trailing the flapping wing is shown in Fig. 16. As expected, the value of Richardson number stays above the Cotel threshold until a particular distance from the core axis; in this case it corresponds to 40% of the core radius of the tip vortex. Within this region the flow inside the

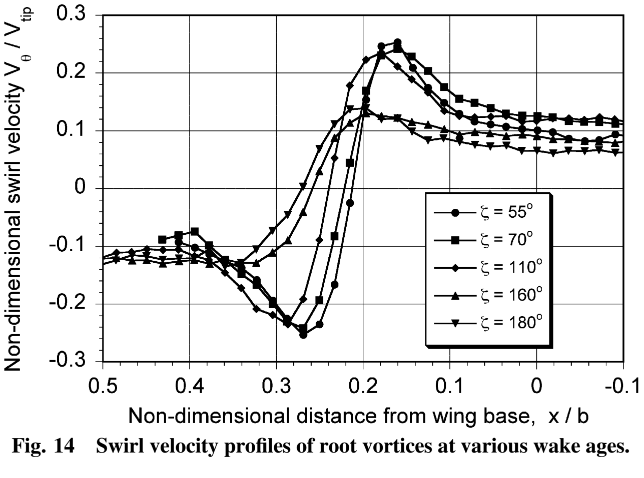

Fig. 14 Swirl velocity profiles of root vortices at various wake ages.

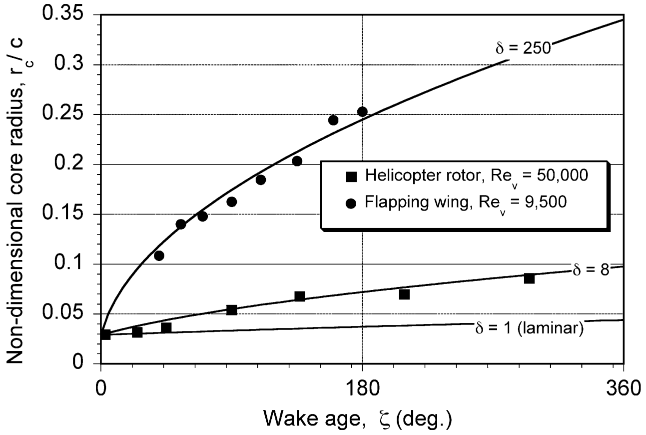

Fig. 15 Comparison of the core growth of tip vortices between a flapping wing and a model-scale rotating-wing.

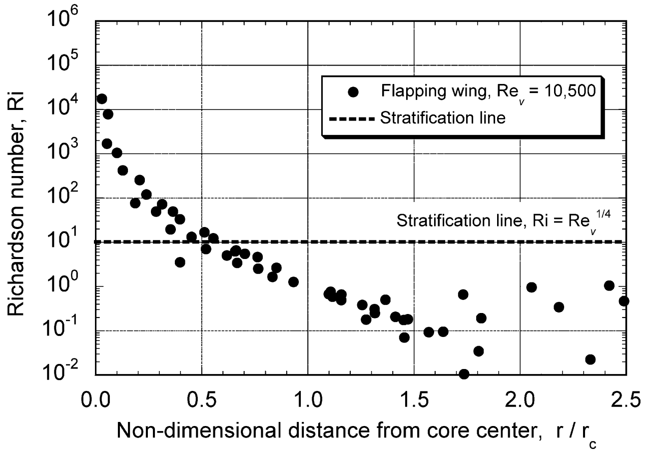

Fig. 16 Variation of Richardson number for a tip vortex trailing a flapping wing.

vortex will remain laminar. However, for the measurements of a rotating wing shown in Fig. 15, it has been shown that the Richardson number stays above the threshold value until 60% of its core radius [32]. This means that the centrifugal forces that prevent the entrainment of turbulence is smaller in the case of flapping wing generated trailed vortices because of the different velocity profiles and the associated smaller velocity gradients near the vortex core. As a result, a larger region of the vortex is susceptible to develop turbulence and, hence, transport vorticity away from the vortex core axis. This will be one source of the increased growth characteristics exhibited by vortices trailing from flapping wings. An accurate measurement of turbulence inside the vortex cores may clearly provide the required insight for a complete explanation of their properties. However, it is clear that a laminar flow assumption made based on the low operating Reynolds number of the flapping wing will not be appropriate.

Conclusions

High-resolution flow visualization and PIV measurements have been performed on a biomimetic flapping-wing concept. The following are the conclusions that have been derived from an analysis of the measured results:

1) The flow features on top of the flapping wing at midstroke were clearly identified. Flow separation appears near the root as well as tip of the wing, with a classic dynamic stall vortex in between. The shedding of the LEV is accompanied by the formation of another shed vortex, resulting in multiple vortices being cast off the wing during the flapping stroke. The presence of at least one vortex over the wing throughout the translation stroke helps explain the sustained lift characteristics shown by flapping wings in the hover condition. The shedding of the vortex occurs despite the presence of a significant component of spanwise flow.

2) The measured strength of the root and tip vortices trailing the flapping wing are large enough to have significant influence on the induced velocity field. The tip vortex is always stronger than the root vortex and was found to be 40% of the maximum velocity of the wing tip at early wake ages. The root and tip vortices move radially toward each other and axially downward with increasing time, with a contracting wake structure suggesting positive lift generation.

3) With increasing time (wake age), the peak swirl velocity of the tip vortex decreases. This is accompanied by an increase in core radius, thereby conserving circulation. The decreasing peak swirl velocity or the increasing viscous core radius is the result of the diffusion of vorticity away from the vortex core, and has its source from the spin down of vortex cores through both viscous and turbulent flow effects.

4) The measured growth rate of the wing tip vortices were found to be much higher than expected, suggesting the presence of greater turbulence inside the vortex cores, despite having very low vortex Reynolds numbers. A Richardson number analysis showed that a larger region of the vortex core is likely to sustain turbulence and to radially transport vorticity away from the vortex. This suggests that scaling effects at these small Reynolds numbers requires further study.

Acknowledgments

This research was supported, in part, by the Multi-University Research Initiative under Grant No. W911NF0410176. The authors wish to acknowledge the contributions of M. J. Tarascio (now with Sikorsky Aircraft Corporation), who built the flapping-wing mechanism. The authors wish to thank Beerinder Singh for his contributions to this work.

References

[1] Bohorquez, F., Samuel, P., Sirohi, J., Pines, D., Rudd, L., and Perel, R., "Design Analysis and Hover Performance of a Rotating Wing Micro Air Vehicle," *Journal of the American Helicopter Society*, Vol. 48, No. 2, April 2003, pp. 80–90.

[2] Ramasamy, M., Leishman, J. G., and Lee, T. E., "Flow Field of a Rotating Wing MAV," *62nd Annual National Forum Proceedings of the American Helicopter Society*, 2006.

[3] Willmott, A. P., Ellington, C. P., and Thomas, A. L. R., "Flow Visualization and Unsteady Aerodynamics in the Flight of the Hawk Moth, Manduca Sexta," *Philosophical Transactions of the Royal Society of London, Series B: Biological Sciences*, Vol. 352, No. 1351, March 1997, pp. 303–316.

[4] Srygley, R. B., and Thomas, A. L. R., "Unconventional Lift-Generating Mechanisms in Free-Flying Butterflies," *Nature (London)*, Vol. 420, Dec. 2002, pp. 660–662.

[5] Buckholz, R. H., "Measurements of Unsteady Periodic Forces Generated by the Blowfly Flying in Wind Tunnel," *Journal of Experimental Biology*, Vol. 90, No. 1, 1981, pp. 163–173.

[6] Zanker, J. M., and Gotz, K. G., "The Wing Beat of Drosophila Melanogaster II. Dynamics," *Philosophical Transactions of the Royal Society of London, Series B: Biological Sciences*, Vol. 327, No. 1238, 1990, pp. 19–44.

[7] Maxworthy, T., "Experiments on the Weis–Fogh Mechanism of Lift Generation by Insects in Hovering Flight. Part I. Dynamics of the Fling," *Journal of Fluid Mechanics*, Vol. 93, No. 1, 1979, pp. 47–63.

[8] Bennett, L., "Clap and Fling Aerodynamics—An Experimental Evaluation," *Journal of Experimental Biology*, Vol. 69, No. 1, 1977, pp. 261–272.

[9] Dickinson, M. H., Lehmann, F. O., and Sane, S. P., "Wing Rotation and the Aerodynamic Basis of Insect Flight," *Science*, Vol. 284, No. 5422, 1999, pp. 1954–1960.

[10] Ellington, C. P., Van den Berg, C., Willmott, A. P., and Thomas, A. L. R., "Leading Edge Vortices in Insect Flight," *Nature (London)*, Vol. 384, No. 6610, 1996, pp. 626–630.

[11] Birch, J. M., and Dickinson, M. H., "The Influence of Wing-Wake Interactions on the Production of Aerodynamic Forces in Flapping Flight," *Journal of Experimental Biology*, Vol. 206, No. 13, 2003, pp. 2257–2272.

[12] Minotti, F. O., "Unsteady Two-Dimensional Theory of a Flapping

Wing," *Physical Review E (Statistical Physics, Plasmas, Fluids, and Related Interdisciplinary Topics)*, Vol. 66, No. 051907, 2002, pp. 1–10.

[13] Wang, Z. J., "Two-Dimensional Mechanism for Insect Hovering," *Physical Review Letters*, Vol. 85, No. 10, 2000, pp. 2216–2219.

[14] Liu, H., and Kawachi, K., "A Numerical Study of Insect Flight," *Journal of Computational Physics*, Vol. 146, No. 1, 1998, pp. 124–156.

[15] Sun, M., and Tang, J., "Unsteady Aerodynamic Force Generation by a Model Fruit Fly Wing in Flapping Motion," *Journal of Experimental Biology*, Vol. 205, 2002, pp. 55–70.

[16] Ramasamy, M., and Leishman, J. G., "Benchmarking PIV Measurements with LDV in the Wake of Hovering Rotor," *25th Applied Aerodynamics Conference, San Francisco, CA*, AIAA Paper No. 2006-3479, June 2006.

[17] Ellington, C. P., "The Aerodynamics of Hovering Insect Flight. IV. Aerodynamic Mechanisms," *Philosophical Transactions of the Royal Society of London, Series B: Biological Sciences*, Vol. 305, No. 1122, Feb. 1984, pp. 79–113.

[18] Weis–Fogh, T., "Quick Estimates of Flight Fitness in Hovering Animals Including Novel Mechanisms for Lift Production," *Journal of Experimental Biology*, Vol. 59, No. 1, 1973, pp. 169–230.

[19] Sane, S. P., "The Aerodynamics of Insect Flight," *Journal of Experimental Biology*, Vol. 206, No. 23, 2003, pp. 4191–4208.

[20] Van den Berg, C., and Ellington, C. P., "The Vortex Wake of a Hovering Model Hawk Moth," *Philosophical Transactions of the Royal Society of London, Series B: Biological Sciences*, Vol. 352, No. 1351, March 1997, pp. 317–328.

[21] Van den Berg, C., and Ellington, C. P., "The Three-Dimensional Leading Edge Vortex of a Hovering Model Hawk Moth," *Philosophical Transactions of the Royal Society of London, Series B: Biological Sciences*, Vol. 352, No. 1351, March 1997, pp. 329–340.

[22] Ellington, C. P., and Usherwood, J. R., "Lift and Drag Characteristics of Rotary and Flapping Wings," *Fixed and Flapping Wing Aerodynamics for Micro-Air Vehicle Applications*, edited by Thomas, A. Mueller, Vol. 195, of AIAA Progress in Aeronautics and Astronautics, AIAA, Reston, VA, 2001, pp. 231–248, Chap. 12.

[23] Birch, J. M., and Dickinson, M. H., "Spanwise Flow and the Attachment of Leading-Edge Vortex on Insect Wings," *Nature (London)*, Vol. 412, No. 6848, 2001, pp. 729–733.

[24] Tarascio, M., Ramasamy, M., Chopra, I., and Leishman, J. G., "Flow Visualization of MAV Scaled Insect Based Flapping Wings in Hover," *Journal of Aircraft*, Vol. 42, No. 2, March 2005, pp. 355–360.

[25] Singh, B., Ramasamy, M., Chopra, I., and Leishman, J. G., "Experimental Studies on Insect Based Biomimetic Flapping Wings For Micro Hovering Air Vehicles," AIAA Paper No. 2005-2293, April 2005.

[26] Singh, B., Ramasamy, M., Chopra, I., and Leishman, J. G., "Insect Based Flapping Wings For Micro Hovering Air Vehicles: Experimental Investigations," *American Helicopter Society International Specialists Meeting on Unmanned Rotorcraft*, 2005.

[27] Leishman, J. G., *Principles of Helicopter Aerodynamics*, Cambridge University Press, New York, 2000, Chap. 9.

[28] Squire, H. B., "The Growth of a Vortex In Turbulent Flow," *Aeronautical Quarterly*, Vol. 16, No. 3, Aug. 1965, pp. 302–306.

[29] Lamb, H., *Hydrodynamics*, 6th ed., Cambridge University Press, Cambridge, 1932, pp. 592–593.

[30] Oseen, C. W., "Uber Wirbelbewegung in einer reibenden Flüssigkeit," *Arkiv for Matematik, Astronomi och Fysik*, Vol. 7, No. 14, 1911, pp. 14–21.

[31] Martin, P. B., Pugliese, G., and Leishman, J. G., "High Resolution Trailing Vortex Measurements in the Wake of a Hovering Rotor," *Journal of the American Helicopter Society*, Vol. 49, No. 1, Jan. 2004, pp. 39–52.

[32] Ramasamy, M., and Leishman, J. G., "A Generalized Model For Transitional Blade Tip Vortices," *60th Annual National Forum Proceedings of the American Helicopter Society*, 2004.

[33] Bradshaw, P., "The Analogy Between Streamline Curvature and Buyoyancy in Turbulent Shear Flows," *Journal of Fluid Mechanics*, Vol. 36, No. 1, 1969, pp. 177–191.

[34] Holzapfel, A., Hofbauer, T., Gerz, T., and Schumann, U., "Aircraft Wake Vortex Evolution and Decay in Idealized and Real Environtments: Methodologies, Benefits and Limitations," *Proceedings of the Euromech Colloquium*, 2001.

[35] Cotel, A. J., and Breidenthal, R. E., "Turbulence Inside a Vortex," *Physics of Fluids*, Vol. 11, No. 10, 1999, pp. 3026–3029.

[36] Cotel, A. J., "Turbulence Inside a Vortex: Take Two," *Physics of Fluids*, Vol. 14, No. 8, Aug. 2002, pp. 2933–2934.